

Evaluation of the ESFR End of Equilibrium Cycle State: Spatial Distributions of Reactivity Coefficients

Baker, U.; Margulis, M.; Shwageraus, E.; Fridman, E.; Jiménez-Carrascosa, A.; García-Herranz, N.; Cabellos, O.; Gregg, R.; Krepel, J.;

Originally published:

August 2021

Journal of Nuclear Engineering and Radiation Science 8(2021)1, 011316

DOI: <https://doi.org/10.1115/1.4052121>

Perma-Link to Publication Repository of HZDR:

<https://www.hzdr.de/publications/Publ-32429>

Release of the secondary publication
on the basis of the German Copyright Law § 38 Section 4.

CC BY

Evaluation of the ESFR End of Equilibrium Cycle State: Spatial Distributions of Reactivity Coefficients

Una BAKER

University of Cambridge
Trumpington St, Cambridge CB2 1PZ, UK
ud215@hermes.cam.ac.uk

Marat MARGULIS

University of Cambridge
Trumpington St, Cambridge CB2 1PZ, UK
mm2353@hermes.cam.ac.uk

Eugene SHWAGERAUS

University of Cambridge
Trumpington St, Cambridge CB2 1PZ, UK
es607@hermes.cam.ac.uk

Emil FRIDMAN

Helmholtz-Zentrum Dresden-Rossendorf (HZDR)
Bautzner Landstraße 400, 01328 Dresden, Germany
e.fridman@hzdr.de

Antonio JIMÉNEZ CARRASCOSA

Universidad Politécnica de Madrid (UPM)
José Gutiérrez Abascal, 2, 28006 Madrid, Spain
antonio.jcarrascosa@upm.es

Nuria GARCÍA HERRANZ

Universidad Politécnica de Madrid (UPM)
José Gutiérrez Abascal, 2, 28006 Madrid, Spain
nuria.garcia.herranz@upm.es

Oscar CABELLOS

Universidad Politécnica de Madrid (UPM)
José Gutiérrez Abascal, 2, 28006 Madrid, Spain
oscar.cabellos@upm.es

Robert GREGG

National Nuclear Laboratory (NNL)
Chadwick House, Warrington WA3 6AE, UK
robert.wh.gregg@nnl.co.uk

Jiri KREPEL

Paul Scherrer Institut (PSI)
5232 Villigen, Switzerland
jiri.krepel@psi.ch

Abstract

The Horizon 2020 ESFR-SMART project investigates the behaviour of the commercial-size European Sodium-cooled Fast Reactor (ESFR) throughout its lifetime. This paper reports work focused on the End of Equilibrium Cycle (EOEC) loading of the ESFR, including neutronic analysis, core- and zone-wise reactivity coefficients, and more detailed local mapping of important safety-relevant parameters. Sensitivity and uncertainty analysis on these parameters have also been performed and a detailed investigation into decay heat mapping carried out.

Due to the scope of this work the results have been split into three papers. The nominal operating conditions and both zone-wise and local mapping of reactivity coefficients are considered in this paper; the sensitivity and uncertainty analysis are detailed in Margulis et al. [1]; and the decay heat mapping calculations are reported in Jimenez-Carrascosa et al. [2].

The work was performed across four institutions using both continuous-energy Monte Carlo and deterministic reactor physics codes. A good agreement is observed between the methods, verifying the suitability of these codes for simulation of large, complicated reactor configurations; and giving confidence in the results for the most limiting ESFR EOEC core state for safety analysis. The results from this work will serve as basis for the transient calculations planned for the next stage of work on the ESFR, allowing for more in-depth studies to be performed on the multiphysics behaviour of the reactor.

1. Introduction

The Horizon 2020 ESFR-SMART (European Sodium Fast Reactor Safety Measures Assessment and Research Tools) is a four-year collaborative project co-funded by European Commission within the Euratom research and training programme [3]. The project was launched to further enhance the safety of the commercial-size European Sodium Fast Reactor (ESFR) investigated in the earlier CP-ESFR project [4].

The neutronic characterisation of the ESFR core at its Beginning of Cycle (BOC) state was performed by Fridman et al. [5, 6] in the preceding project task. This work included an evaluation of safety-related neutronic parameters for the fresh core, as well as once-through and realistic batch-wise burnup analysis aimed at establishing the equilibrium core loading pattern. This task also provided the core set-up and material balances at the End of Equilibrium Cycle (EOEC) state. The detailed core geometric specifications were provided by previously published work on the ESFR by Mikityuk et al. [7]. A brief description is included here for clarity, with a focus on the EOEC parameters.

The aim of this project task was to evaluate the safety-relevant neutronic parameters at the EOEC state for comparison with the BOC results and to characterise the global and local behaviour of the Doppler constant and sodium void worth. Following this, uncertainty and sensitivity analyses were carried out and an analysis of spatial distributions of decay heat. These additional investigations are detailed separately [1, 2].

2. ESFR Core Description

The core is split into two radial zones: the inner fuel (IF) and the outer fuel (OF), containing 216 and 288 assemblies respectively. Each radial zone is divided into a six-batch loading pattern as shown in Figure 1. The core reactivity is regulated by 24 control and shutdown devices (CSD) and 12 diverse shutdown devices (DSD). The ESFR-SMART core contains 31 corium discharge tubes (CDT) to ensure that no corium remains in the core during a meltdown. These include the central position, the boundary between the inner- and outer- zones, and the boundary between the outer-zone and the reflector. Outside the radial reflector the ESFR-SMART design contains positions for storage of irradiated fuel, which are empty in the model used here. The 108 S1 positions are dedicated for the IF assemblies while the 144 S2 positions are reserved for the OF assemblies. Finally, the core is surrounded by four rings of bio-shielding. It should be noted that previous analysis in the project showed that the empty spent fuel positions have no effect on the core neutronics and thus can be neglected in the core analysis [5, 6].

The axial layout of the IF and OF assemblies is presented in Figure 2. The active region (marked by the dashed red square in Figure 2) was further divided into several burnable regions to account for exposure to different neutron fluxes. The IF assembly was divided into 3 axial nodes in the lower fertile region and 5 nodes in the upper fissile region. The OF assembly contained a single axial node in the fertile region due to its shorter length in comparison to the IF assembly. The fissile region of the OF assembly was divided into 5 axial nodes, similar to the IF assembly, with slightly longer nodes. This mesh was used in the detailed maps, presented in Section 6.

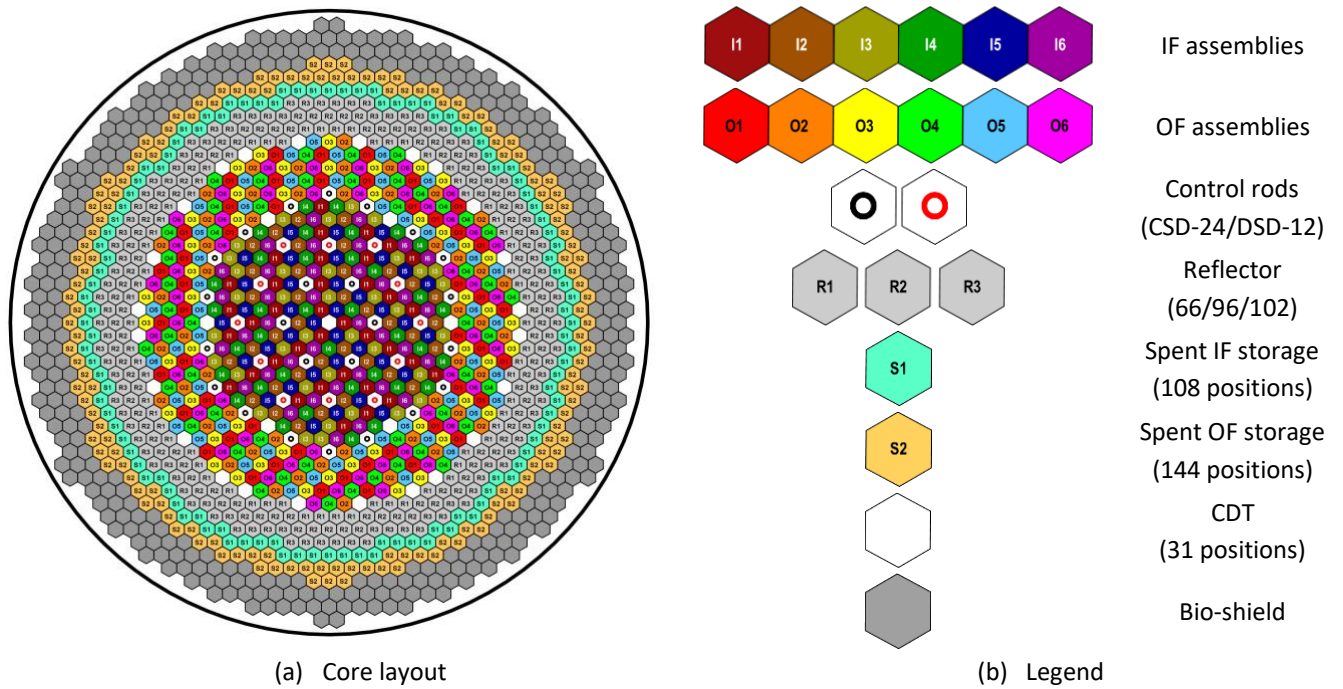


Figure 1 - ESRF-SMART core loading pattern

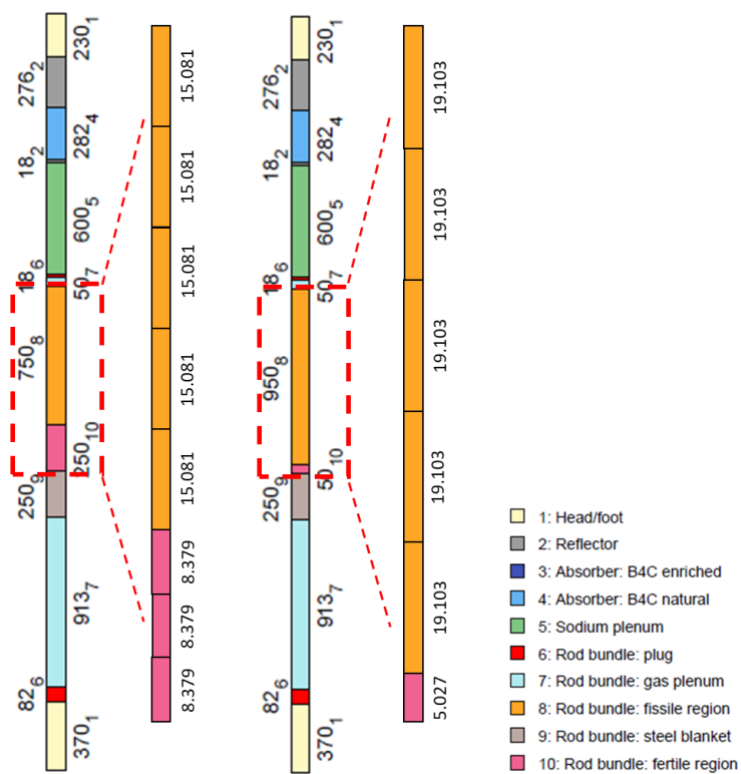


Figure 2 - Axial layout of IF (left) and OF (right) assemblies

The EOE condition for the ESRF-SMART core was discussed at length in the preceding BOC analysis. The 6-batch core management scheme was proposed to reduce power peaking and reactivity variation between the batches. The in-core residence time for each batch was fixed to 2172 days and each fuel cycle length was set to 362 days at full power. The EOE core was established at the end of three full in-core residence periods per batch (18 successive fuel cycles), with control rods at their parked position. This depletion calculation was performed in the previous ESRF-SMART project task [5, 6], providing the detailed fuel compositions used for this work.

3. Modelling assumptions

The neutronic calculations were performed assuming uniform temperature in each zone. The adopted temperature values are shown in Table 1.

Table 1 - Nominal material temperature

Zone	Material	Temperature, K
IF	Fissile	1500
	Fertile	900
	Sodium	900
	Structure material	900
OF	Fissile	1500
	Fertile	900
	Sodium	900
	Structure material	900

The aim of this work was to examine how the ESRF core behaviour changed through its lifetime. The EOEC state was compared to the previous BOC state analysed by Fridman et al. [5, 6] by comparing a variety of parameters from the fresh core with the burnt core:

- Core reactivity at nominal conditions
- Control rod worth and reactivity curve
- Sodium void reactivity
- Doppler constants

3.1 Control rod worths

The control rod worth and reactivity curve was calculated as the difference in reactivity between the nominal and the fully rodded states. At the nominal state, all CSD and DSD rods are withdrawn to their parking position (the top of the upper gas plenum). When inserted, the upper part of the control rod aligns with the top of the fissile zone, below the upper gas plenum, as shown in Figure 3.

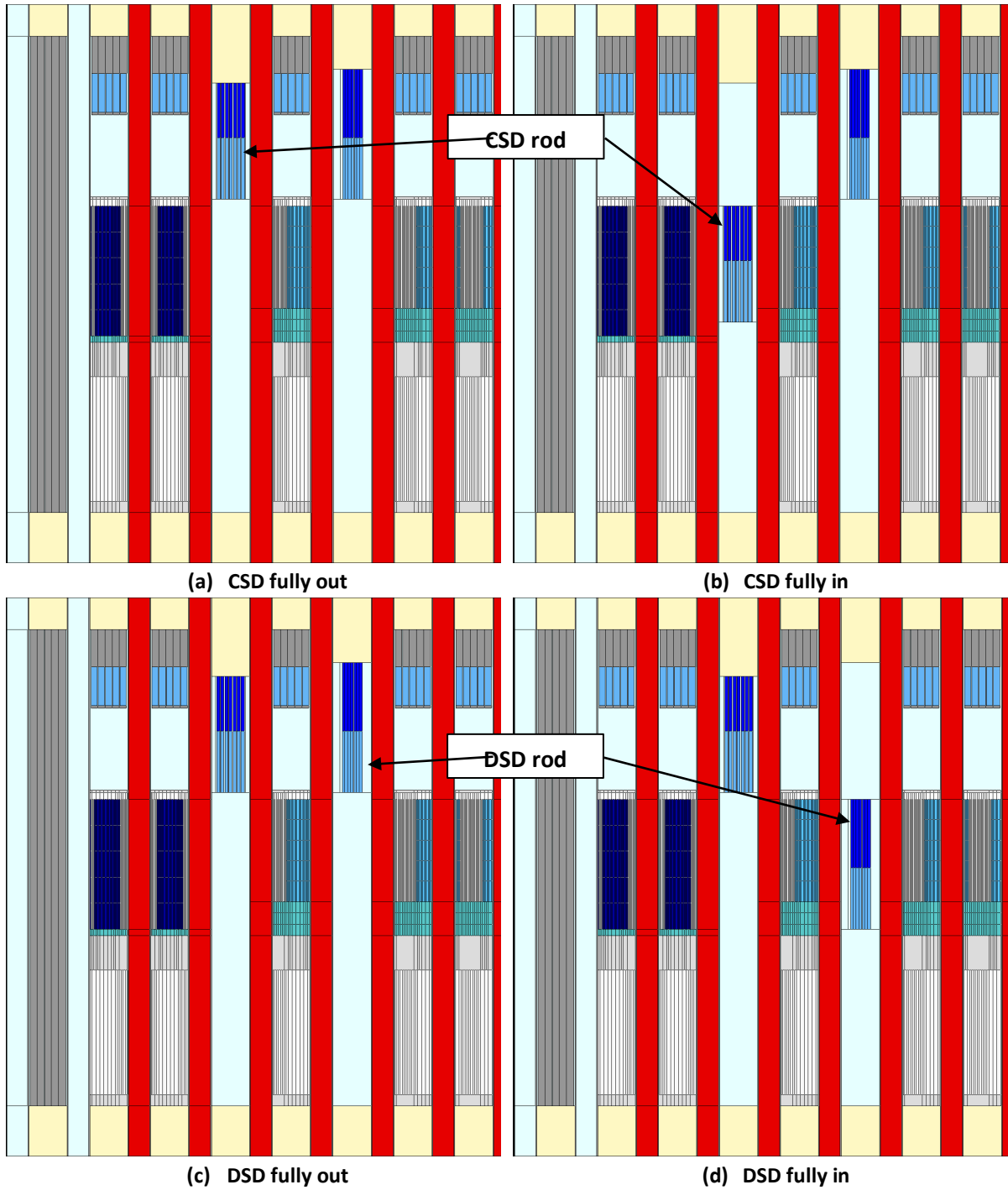


Figure 3 - Core axially cut to show control rod positions

3.2 Doppler constants

The local Doppler constants were calculated for three zones: inner fissile, outer fissile, and all the fertile zones, across three temperature ranges (300K to 600K, 900K to 1200K, and 1500K to 1800K) as shown in Table 2.

Table 2 - Zone-wise temperature variation for Doppler constants estimation

Description	T inner fissile (K)	T outer fissile (K)	T inner + outer fertile (K)	T structure (K)	T B4C (K)
Reference	300/900/1500	300/900/1500	300/900/1500	300/600/900	300/600/900
Inner fuel high temp	600/1200/1800	300/900/1500	300/900/1500	300/600/900	300/600/900
Outer fuel high temp	300/900/1500	600/1200/1800	300/900/1500	300/600/900	300/600/900
Fertile fuel high temp	300/900/1500	300/900/1200	600/1200/1500	300/600/900	300/600/900

3.3 Sodium void reactivity

Sodium void reactivity was calculated as the difference in reactivity between nominal and voided states. The BOC analysis defined the following cases (noted as Void 1 to 5 in Figure 4):

- Void 1 – voiding of inner fissile region
- Void 2 – voiding of outer fissile region
- Void 3 – voiding of everything above the inner fissile region
- Void 4 – voiding of everything above the outer fissile region
- Void 5 – a combination of void cases 1 to 4 (inner and outer zones and everything above)

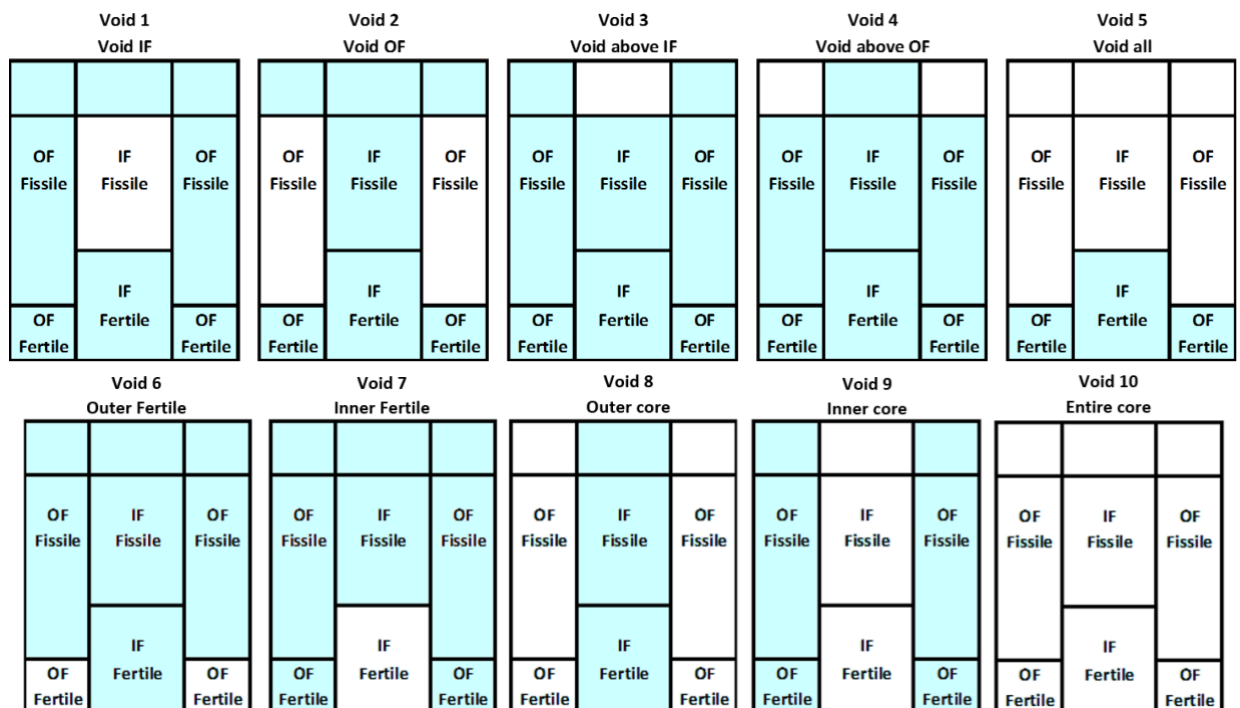


Figure 4 – Zone-wise sodium void maps

In addition to the cases mentioned above, five extra sodium cases were added. The BOC analysis found that the power in the outer and inner lower fertile zones rises significantly with burnup as fissile materials are bred. The lower fertile zones may therefore have similar characteristics as the upper fissile regions at EOEC and sodium voiding in these zones could lead to a positive reactivity effect. The following sodium void cases were added in this work:

- Void 6 – voiding of the outer fertile region

- Void 7 – voiding of the inner fertile region
- Void 8 – voiding of the entire length of the outer region
- Void 9 – voiding of the entire length of the outer region
- Void 10 – voiding of the entire core

It should be noted that the inter-assembly gaps were not emptied of sodium.

3.4 Thermal expansion effects

The simulations also considered the possibility of thermal expansion of different elements in the core:

- Cases 1 and 2 – Axial fuel expansion in the inner and outer core regions (cladding remained constant)
- Cases 3 and 4 – Axial cladding expansion in the inner and outer core regions (fixed fuel geometry)
- Cases 5 and 6 – Radial cladding expansion in the inner of outer core regions (fixed fuel geometry)
- Case 7 - Diagrid expansion

4 Simulation Methods

The calculations were carried out by four organisations using both continuous energy Monte Carlo (MC) and deterministic transport (DT) codes. The code hierarchy is presented in Table 3. With the exception of WIMS-11, which uses a specialised JEFF-3.1.2 evaluation, all the other codes use JEFF-3.1 [8] as reference nuclear data library.

Table 3 – Organisations and codes

Organisation	Code	Solver	Nuclear data library
University of Cambridge	Serpent 2.1.29/2.1.31 [9]	MC	JEFF-3.1
Helmholtz-Zentrum Dresden-Rossendorf	Serpent 2.1.29/2.1.31	MC	JEFF-3.1
Universidad Politécnica de Madrid	KENO-VI [10]	MC	JEFF-3.1
National Nuclear Laboratory	WIMS-11 [11]	DT	JEFF-3.1.2
Paul Scherrer Institut (PSI)	ERANOS/VARIANT [12]	DT	JEFF-3.1

All MC codes perform direct 3-dimensional full-core calculations using the most detailed representation of the ESRF core geometry. However, there is a slight difference in the computational approach between Serpent and KENO which arises due to the no consideration of probability tables for the unresolved resonance range in KENO because of issues found during JEFF-3.1 AMPX processing [19]. These are included in Serpent using the *ures* option.

4.1 WIMS-11

WIMS is a deterministic reactor physics code developed by the ANSWERS team at Jacobs [13]. The 3D diffusion solver MERLIN has been used for this work with assembly-homogenised cross-sections generated using the WIMSECCO fine-group starting module and the CACTUS method of characteristics sub-solver. The super homogenisation method is used to correct the control rod homogenised cross-sections [14]. WIMS treats unresolved resonances using resonance integrals in the equivalence theory method.

4.2 ERANOS

ERANOS 2 is an optimized deterministic calculation system [15] consisting of several modules. The results presented in this report were based on cell level cross-section calculation with ECCO module using standard calculation route passing through 1968 energy group step and using the JEFF3.1 cross-section library. The hexagonal-z flux calculation was accomplished with nodal variational transport module VARIANT using 33 neutron group structure. Compared to other codes, the fuel burnup distribution at EOEC state was obtained also by ERANOS simulation using the EQL3D procedure [16] to simulate the reactor batch-wise operation.

5 RESULTS – NEUTRONIC CALCULATIONS

This section presents the results of the EOEC core neutronic calculations provided by the contributing organisations. In total 52 simulation cases are considered:

- Cases 1-12 deal with the rod insertion
- Cases 13-30 summarize the Doppler constants evaluation
- Cases 31-40 consider sodium voiding scenarios
- Cases 41-52 examine the thermal expansion.

All the presented relative errors in this section are reported with respect to the Serpent results unless stated otherwise.

5.1 Control rod insertions

Fig. 5 compares the integral reactivity worth of the control rods, while Fig. 6 compares the differences between the code predictions. KENO and WIMS agree well with the S-curve obtained by Serpent, with most of the insertion step errors below 50 pcm (Fig. 6a). A slightly higher deviation is noted in WIMS for when the rods reach their final position (about 100 pcm at Step 11).

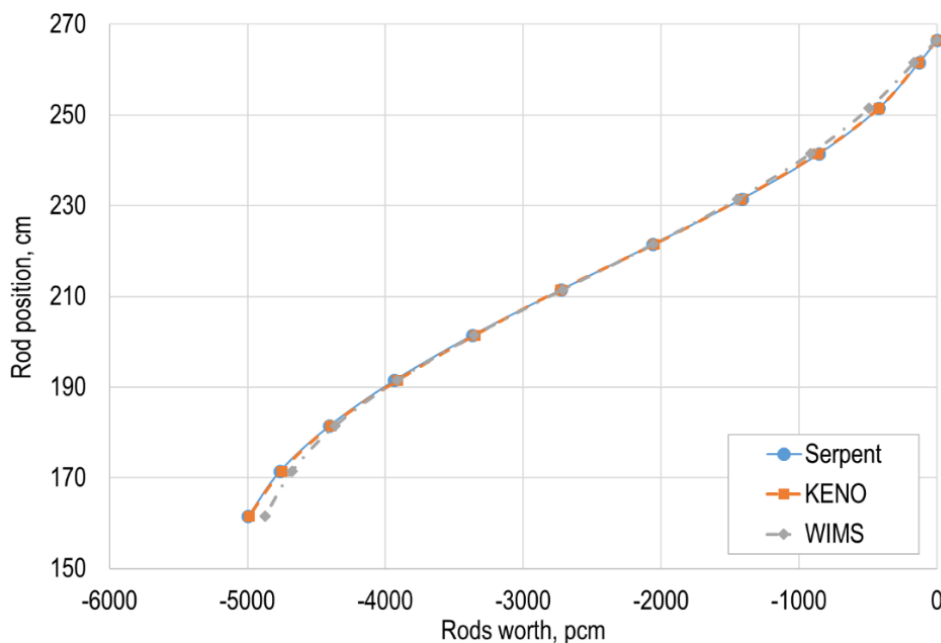


Figure 5 - Control rod insertion S-curve

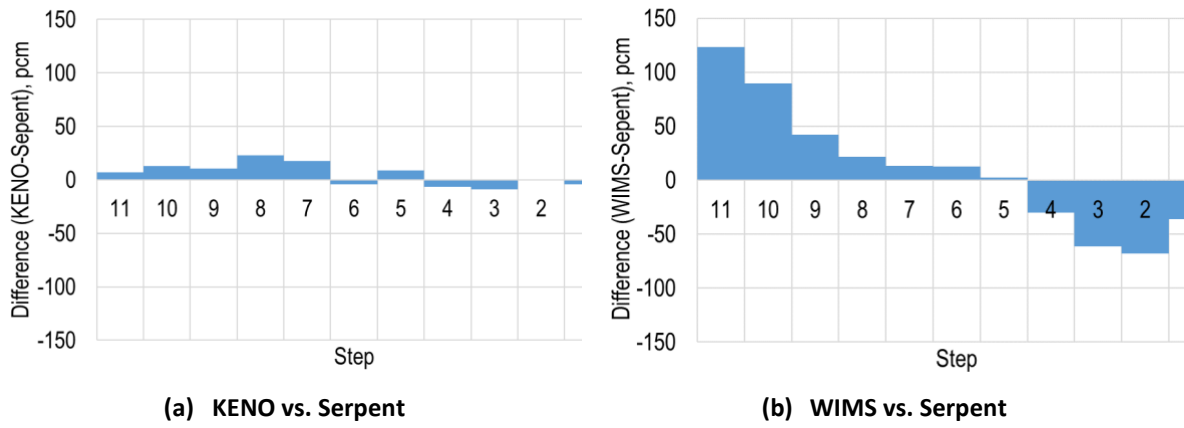


Figure 6 – Different in evaluations of the control rod insertion S-curve

5.2 Doppler constants

The estimated Doppler constants are shown in Fig. 10. In total, nine cases were examined:

- Cases 1-3: temperature variation from 300K to 600K in the inner fissile (case 1), outer fissile (case 2), and all the fertile zones together (case 3).
- Cases 4-6: temperature variation from 900K to 1200K in the inner fissile (case 4), outer fissile (case 5), and all the fertile zones together (case 6).
- Cases 7-9: temperature variation from 1500K to 1800K in the inner fissile (case 7), outer fissile (case 8), and all the fertile zones together (case 9).

Serpent simulations show that the Doppler constant in all the areas drops with the increase of temperature as expected. The inner and outer fissile zones have roughly the same magnitude of the Doppler constant. KENO results deviate from the trend observed in Serpent (with and without *ures*) and WIMS results. The mid-temperature range (900K-1200K) is associated with the lowest estimated Doppler constant. However, the statistical error in KENO is about 2-3 times higher than the error of the results obtained by Serpent. Most of the differences, shown in Fig. 10b, can be explained by the high statistical error and the lack of resonance probability tables in KENO as disabling the *ures* option in Serpent drastically reduces the difference between KENO and Serpent. The largest deviation is observed in Case 6, where the KENO Doppler is estimated to be positive.

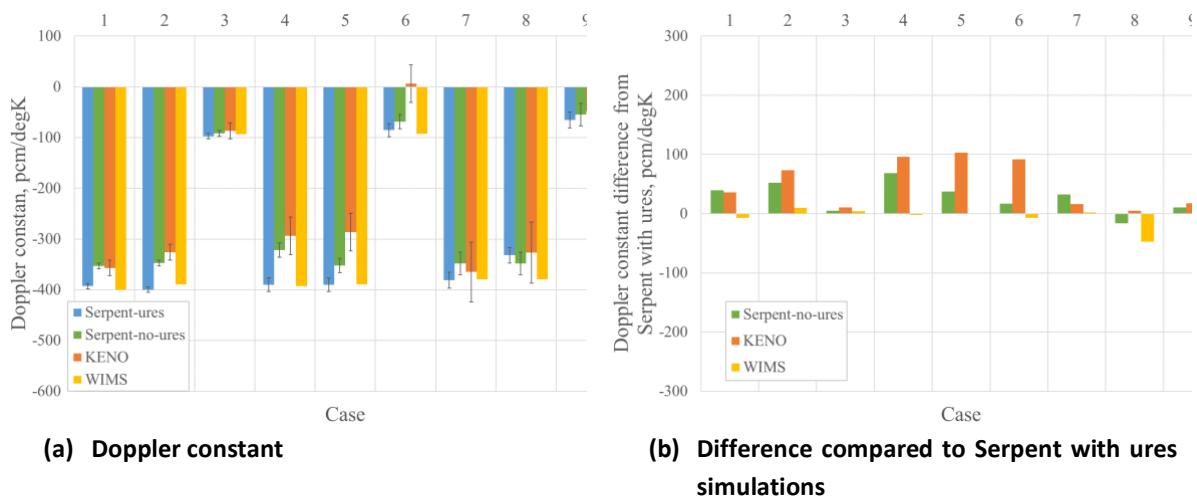


Figure 7 - Doppler constant comparison

5.3 Sodium void worths

The sodium void reactivity worths are shown in Fig. 11 for the different void cases as presented in Fig. 4. The void trends follow a similar pattern to the core behaviour at BOEC [5, 6] with one exception in Case 5 (Fig. 11a).

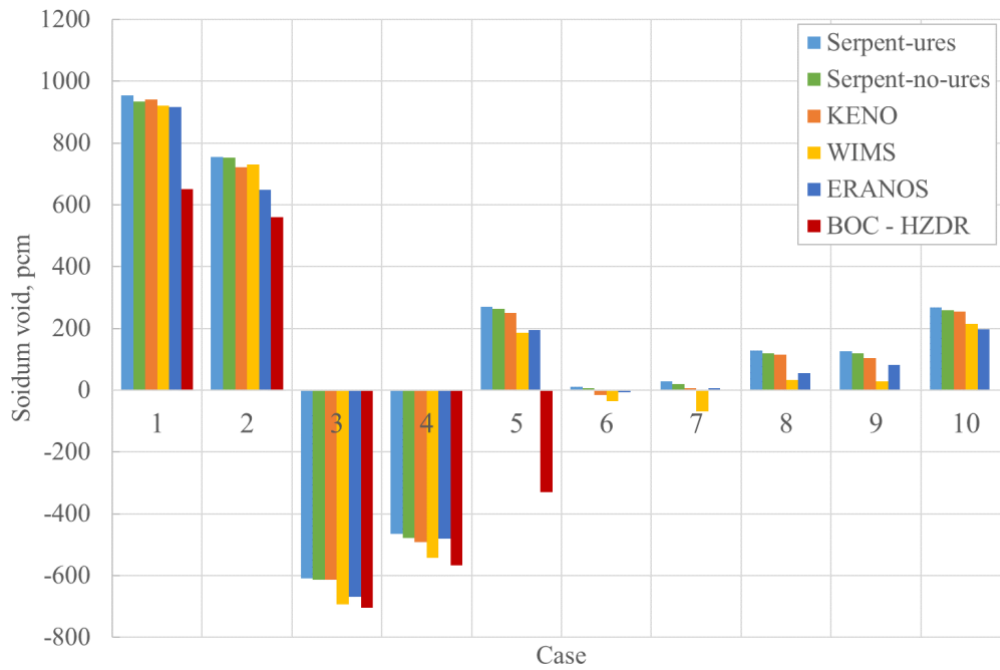
The voiding of inner and outer fissile zones (Cases 1 and 2) results in a large positive reactivity effect. This effect is higher by about 40-50% in respect to BOC conditions, due to the fissile material increase in the fissile region at EOEC. This can be seen in Fig. 12, which shows the change in Pu-239 concentration in each batch of the inner and outer fuel as an example. The different codes are in a good agreement for these two cases with well below 50 pcm between them, with only ERANOS underestimating the outer fissile zone void by about 100 pcm (Fig. 4).

The EOEC lower fuel zone is addressed as fertile for consistency, even though fissile material is bred there during the cycle. The void effect from this zone is slightly less negative in respect to the same value at BOC (Fig. 4a), which is due to the breeding of fissile material in the fertile zones. In these cases Serpent and KENO agree within 20 pcm, while ERANOS and WIMS agree within 80 pcm with the Serpent simulations.

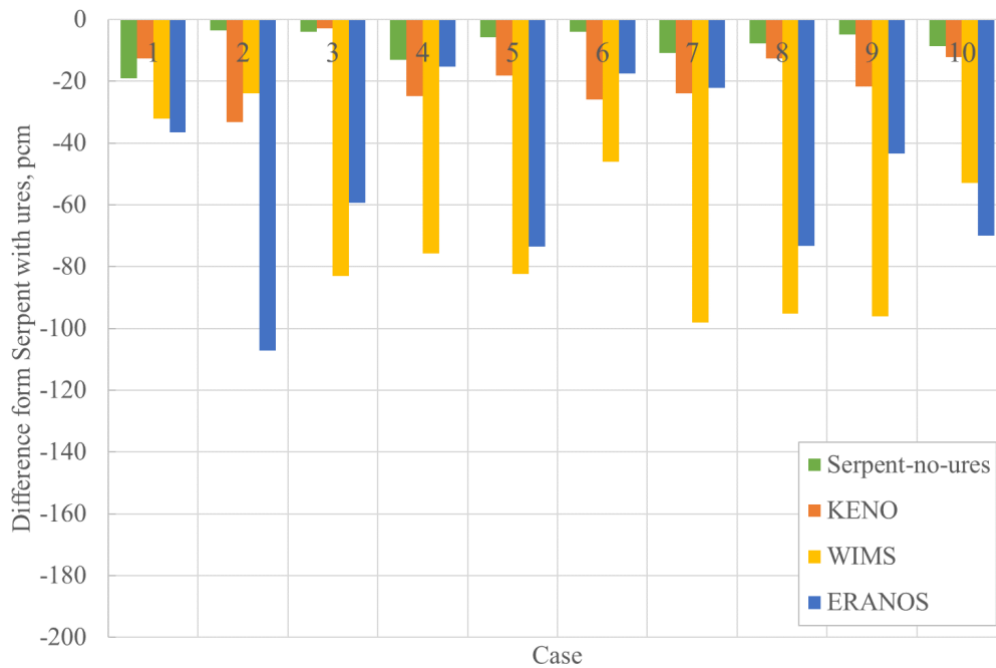
The voiding of the fissile zone and the sodium plenum simultaneously (Case 5 in Fig. 4) results in a negative total void reactivity worth at BOEC. However, for the same configuration at EOEC, the void reactivity worth is strongly positive. The change in void behaviour is credited to the breeding of plutonium. Fig. 12 shows the Pu-239 concentration in each batch of fissile fuel in the inner and outer core. Except for Batch 1 (in both inner and outer), all the other batches have gained plutonium at EOEC. As plutonium is bred in the lower fertile regions, the neutron flux and neutron importance are shifted downwards in the core. A consequence of this is that when the plenum is voided, the additional leakage component added at the top of the core is less important and produces a smaller negative feedback. Monte Carlo codes were found to be in a good agreement, within around 20 pcm, while the deterministic codes deviate from the reference MC solution by about 80 pcm.

At EOEC some of the power is generated in the fertile zones due to the plutonium breeding throughout the cycle, which can lead to sodium boiling in those zones. The EOEC sodium void worth analysis includes voiding of the fertile zones separately (Cases 6 & 7), along with the fissile zone and plenum (Cases 8 & 9), and entire core void (Case 10), as shown in Fig. 4.

The results of Cases 6 to 10 are shown in Fig. 11. The Monte Carlo codes agree within 20 pcm, while WIMS and ERANOS stay within 100 pcm. Only Case 6 has a slight disagreement between the codes, with the Serpent simulation predicting a slight positive void contribution, while the other codes predict a negative value. This is attributed to the small values with high statistical error.

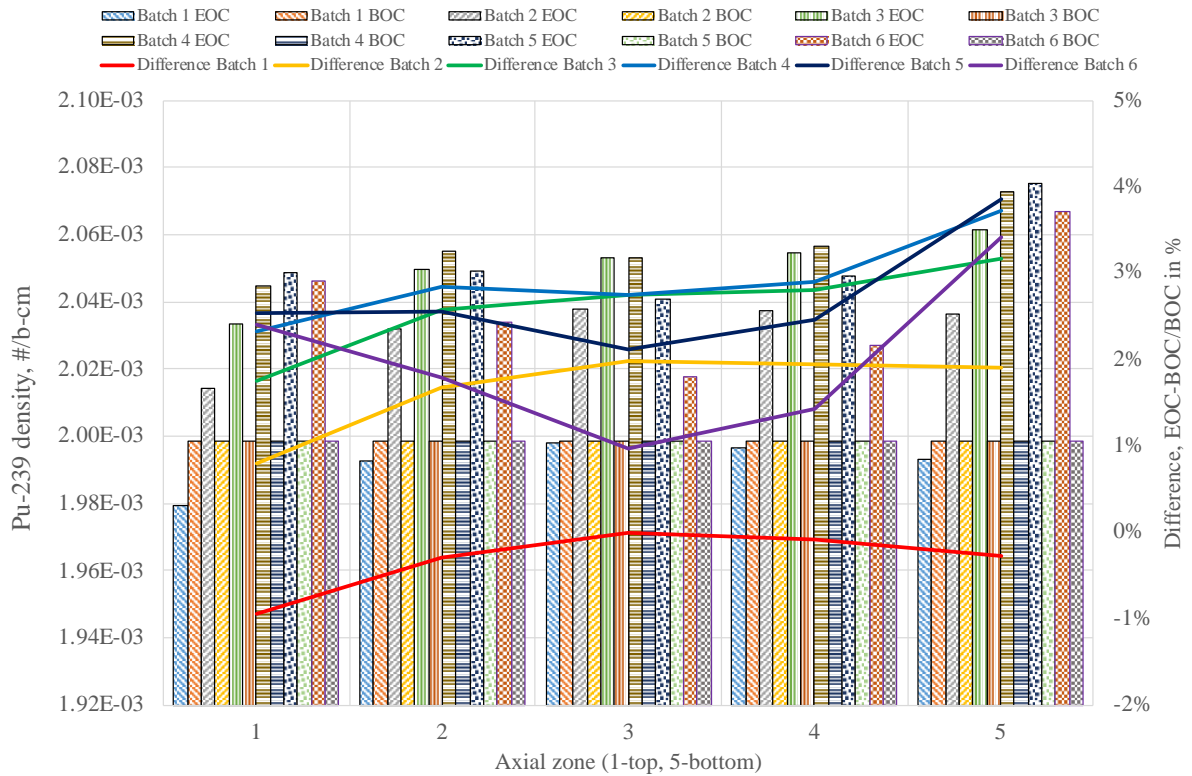


(a) Sodium void worth cases

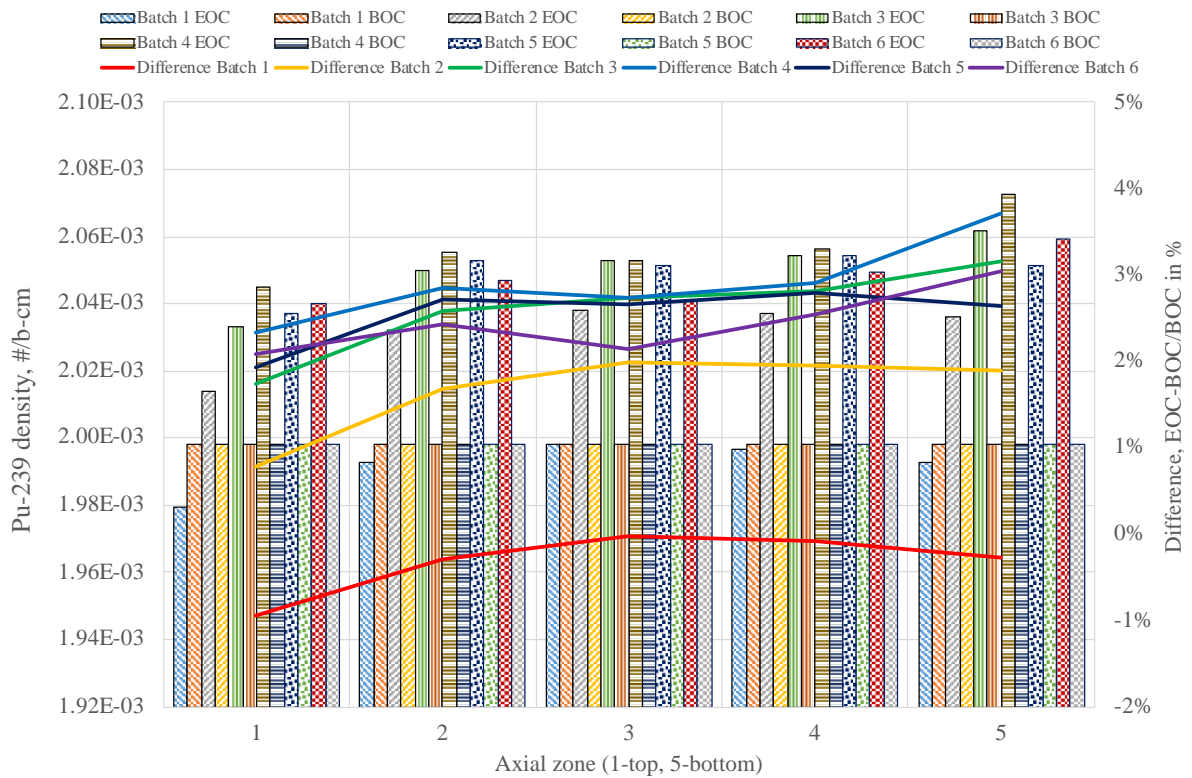


(b) Differences in sodium void reactivity vs. Serpent with ures

Figure 11 - Zonal sodium void worth for different cases shown in Fig. 4.



(a) Inner fuel



(b) Outer fuel

Figure 12 - Plutonium concentration compared with BOC.

Although the strongly positive void reactivity seen in Case 5 of Fig. 11a is at first glance highly undesirable, it should be noted that the scenario presented is not realistic as it considers the voiding

of the whole of the core and plenum together simultaneously. A more physical scenario would be to void the plenum and only part of the top section of the fuel in a manner representative of initial boiling.

It is important to note the spatial correlation effects appearing when voiding neighbouring regions simultaneously. It can be verified that the sodium void worth in Case 5 (269 pcm – Serpent ures in Fig. 11) differs from the sum of individual sodium void worths in Cases 1 to 4 (633 pcm – Serpent ures in Fig. 11), although it corresponds to the voiding of the same zones together. This is due to the strong correlation between the upper active core and the sodium plenum, further discussed in [17] and illustrated in Fig. 13. The upper 25cm of the active core and the plenum were voided in corresponding steps of 20% using the ERANOS code. The results are shown below in Fig. 13.

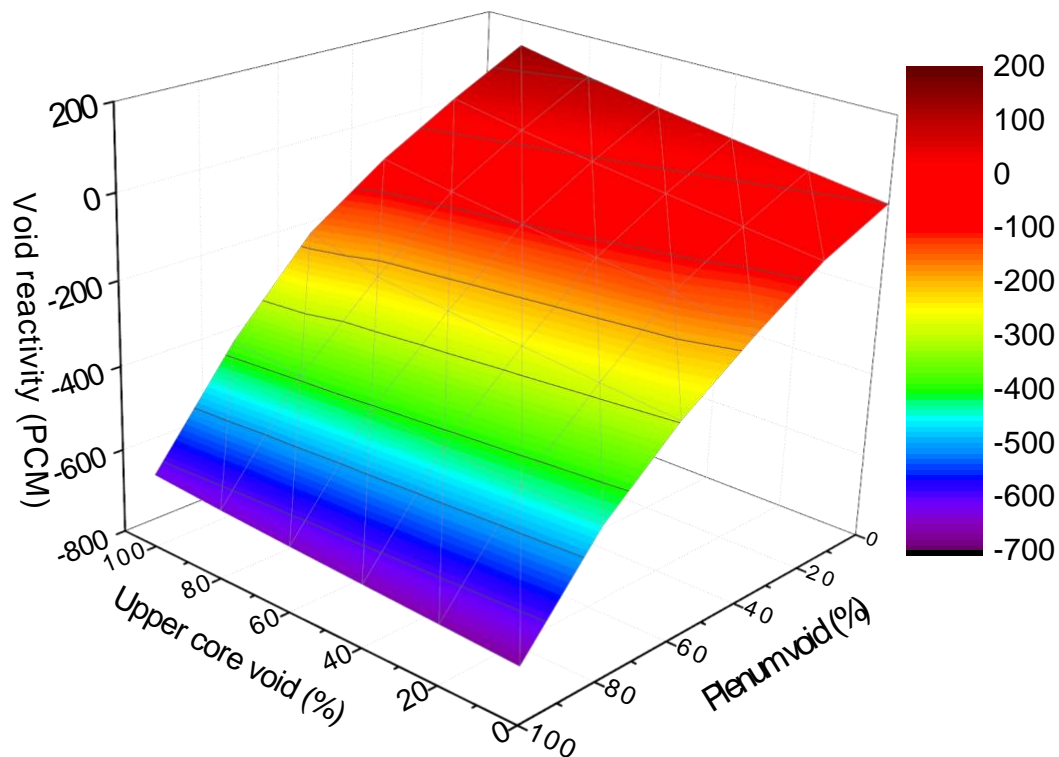
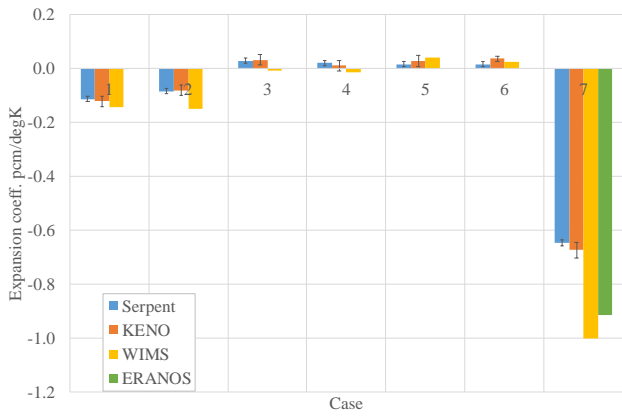


Fig. 13 – Void reactivity as a function of the top fuel zone and plenum void

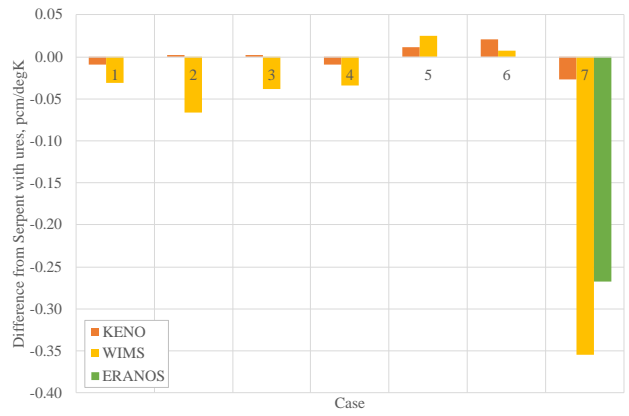
In this more realistic scenario, when the top ~25% of the core and the whole plenum are voided, the void reactivity remains negative. As such it is not concerning that the non-realistic Case 5 showed a positive void reactivity, as the core safety should not be compromised provided downward propagation of the void is prevented.

5.4 Thermal expansion effects

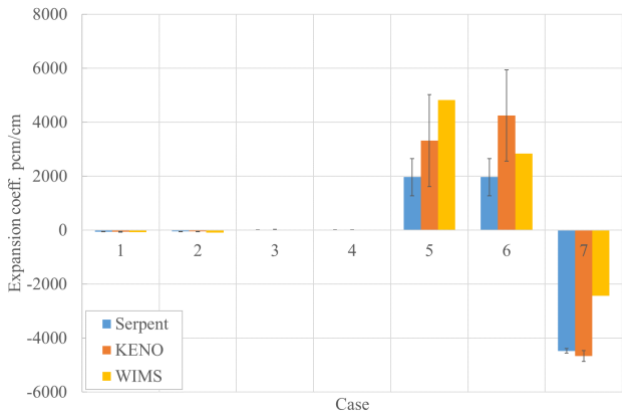
The results of the thermal expansion coefficients are summarised in Fig. 14. It can be observed that the results obtained by Serpent and KENO do not agree on most of the cases. The most notable discrepancies are in the radial cladding expansion (Cases 5 & 6) and the diagrid expansion (Case 7) in Fig. 14. However, most of the coefficients are relatively small in magnitude. The main reason for the large expansion coefficient in pcm/cm is the small change in the dimension. We propose that this is mainly an artefact of normalization and the difference between Serpent and KENO is within the statistical deviation of the two codes.



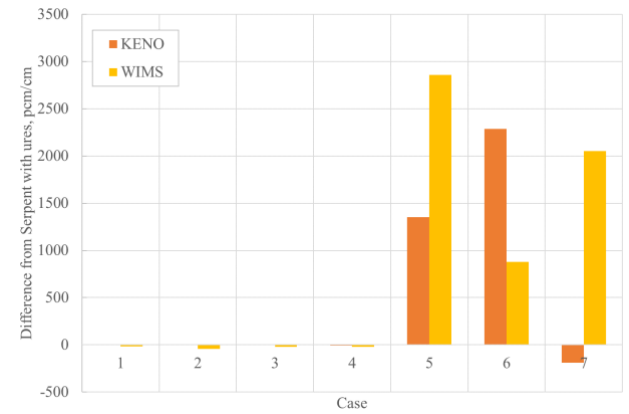
(a) In pcm/K



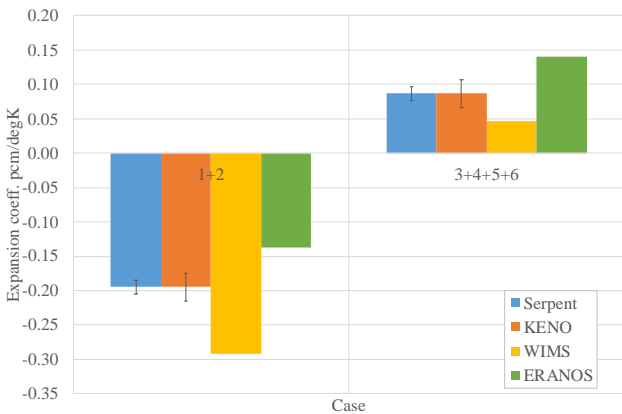
(b) Diff. from Serpent in pcm/K



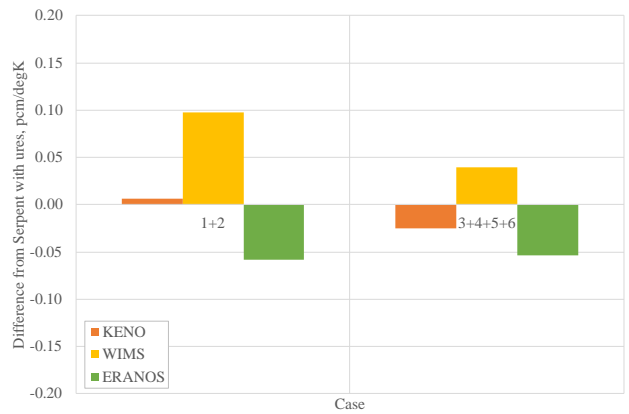
(c) In pcm/cm



(d) Diff. from Serpent in pcm/cm



(e) Combined fuel (1+2) & cladding (3+4+5+6) in pcm/K



(f) Diff. from Serpent in pcm/K

Figure 14 - Thermal expansion coefficient.

The WIMS results are consistent with the Monte Carlo results with slight deviations and the normalized results per degree Kelvin are of the same magnitude with relatively low error in respect to the Serpent calculations. This slight deviation could also be attributed to the use of a different nuclear data library in WIMS (JEFF-3.1.2 vs. JEFF-3.1).

The ERANOS results were calculated slightly differently due to the use of a different modelling approach. Instead of finding the thermal expansion effects for all individual cases, three calculations were performed: the total fuel expansion effect (equivalent to Cases 1 & 2 together); the total clad expansion effect (equivalent to Cases 3, 4, 5 & 6 together); and the diagrid expansion effect (Case 7). Case 7 may be compared directly to the other single-case results, but to evaluate the two combined

calculations the sum of the individual case results for the other codes was taken to find the total fuel and total cladding expansion effects. This can be seen in Fig. 14e. It should be noted that simply taking the sum of the individual perturbations may not provide the same effect as performing all the perturbations at once due to spatial correlations within the core. The whole perturbation is greater than the sum of the partial perturbations, which could explain the slight difference observed between the ERANOS results and the summed results from the other codes.

6 Global and Local Parameter Calculation Methodology

Global parameters were determined by isolating the different regions of the core and considering them separately for the Doppler constant and sodium void worth analysis. For transient analysis, a further discretisation of the core space is required. The core was divided into 5 radial cooling groups (Fig. 15) with several axial nodalisation schemes based on the utilized code and the parameter under investigation.

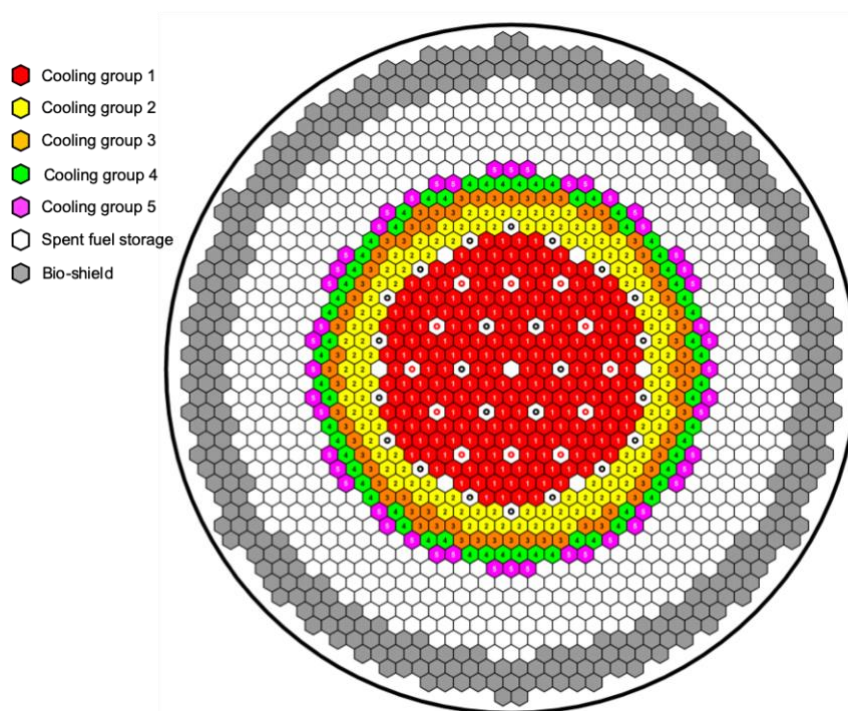


Figure 85 - Radial cooling group distribution

6.1 Global Doppler constants

Doppler constants were calculated for the entire core, inner core only, and outer core only, with fissile and fertile regions considered separately for each section. These calculations were then repeated with a core voided of sodium.

The cases and temperature perturbations are presented in Table 4.

Table 4 - Cases for global Doppler constant analysis

Case No.	Description	T inner fissile	T outer fissile	T fertile inner	T fertile outer	T struct.	T B4C	Sodium void
1	Reference 1	1500	1500	900	900	900	900	0%
2	Whole core - total	1800	1800	1200	1200	900	900	0%
3	Whole core - fissile	1800	1800	900	900	900	900	0%

4	Whole core - fertile	1500	1500	1200	1200	900	900	0%
5	Inner core - total	1800	1500	1200	900	900	900	0%
6	Inner core - fissile	1800	1500	900	900	900	900	0%
7	Inner core - fertile	1500	1500	1200	900	900	900	0%
8	Outer core - total	1500	1800	900	1200	900	900	0%
9	Outer core - fissile	1500	1800	900	900	900	900	0%
10	Outer core - fertile	1500	1500	900	1200	900	900	0%
11	<i>Reference 2</i>	<i>1500</i>	<i>1500</i>	<i>900</i>	<i>900</i>	<i>900</i>	<i>900</i>	<i>100%</i>
12	Whole core - total	1800	1800	1200	1200	900	900	100%
13	Whole core - fissile	1800	1800	900	900	900	900	100%
14	Whole core - fertile	1500	1500	1200	1200	900	900	100%
15	Inner core - total	1800	1500	1200	900	900	900	100%
16	Inner core - fissile	1800	1500	900	900	900	900	100%
17	Inner core - fertile	1500	1500	1200	900	900	900	100%
18	Outer core - total	1500	1800	900	1200	900	900	100%
19	Outer core - fissile	1500	1800	900	900	900	900	100%
20	Outer core - fertile	1500	1500	900	1200	900	900	100%

6.2 Local Doppler constants

The nodalisation scheme for the local Doppler calculations includes 3 fertile (FE) and 5 fissile (FI) nodes in the inner core section (IF), with a single fertile zone (FE) and 5 fissile zones (FI) in the outer core section (OF). ERANOS used an equal-node scheme with 20 separate nodes, as shown in Fig. 16.

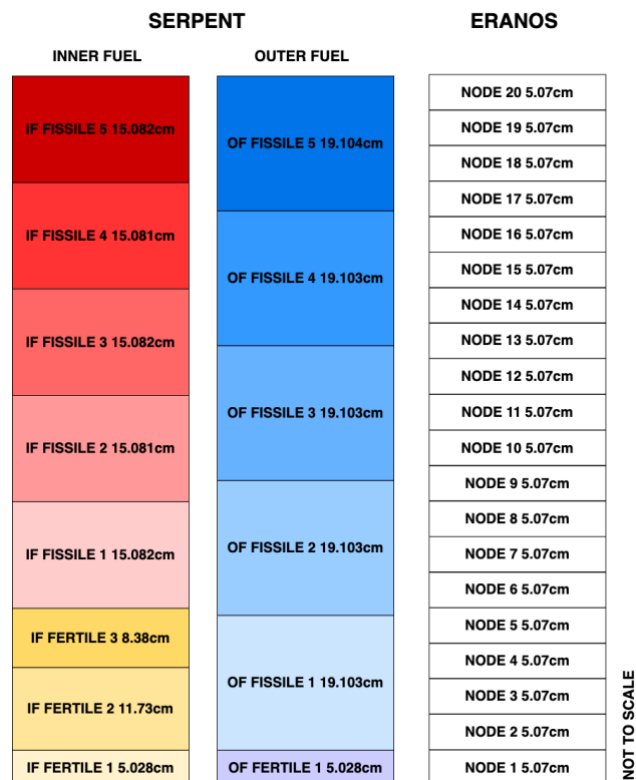


Figure 16 – Axial nodalisation of Serpent and ERANOS for Doppler calculations

6.3 Global sodium void worth

Sodium void simulations were carried out in three steps. Firstly, the core and the plenum were voided simultaneously. Secondly, only the core active zone was voided. Finally, only the plenum void effects were studied. The voiding of the core was done in several steps and initially the sodium density effect was examined without boiling. This was followed by simulations where boiling had occurred.

6.4 Local sodium void worth

The radial nodalisation for the local sodium void worth calculations is the same as the one presented in Fig. 15, consisting of five radial cooling groups. The axial nodalisation is shown in Fig. 17 and is once more similar to the Doppler Effect cases, with the addition of nodes associated with the sodium plenum. In total, there are six additional nodes in Serpent and ERANOS.



Figure 17 – Axial nodalisation of Serpent and ERANOS for sodium worth calculations

7 RESULTS – GLOBAL AND LOCAL ANALYSIS

7.1 Global Doppler constant

The global Doppler constants estimated by Serpent and ERANOS are summarised in Fig. 18. The results show a difference of about 200 pcm/K in the “whole core plus plenum” simulation (Cases 2 and 12) between Serpent and ERANOS. The difference also holds for the voiding of the fissile zone (Cases 3 and 13). On the other hand, the difference disappears when only the fertile zone temperature is perturbed (Cases 4 and 14). The same trends are observed when only the inner core (Cases 5-7 and 15-17) and outer core (Cases 8-10 and 18-20) are considered, with a lower difference with respect to

the full core (about 100 pcm/K). It should be noted that the two simulations adopted different temperature differences. Serpent results were normalized to $-\ln\left(\frac{1800}{1500}\right)$, while ERANOS results were normalized to $-\ln\left(\frac{2500}{1500}\right)$.

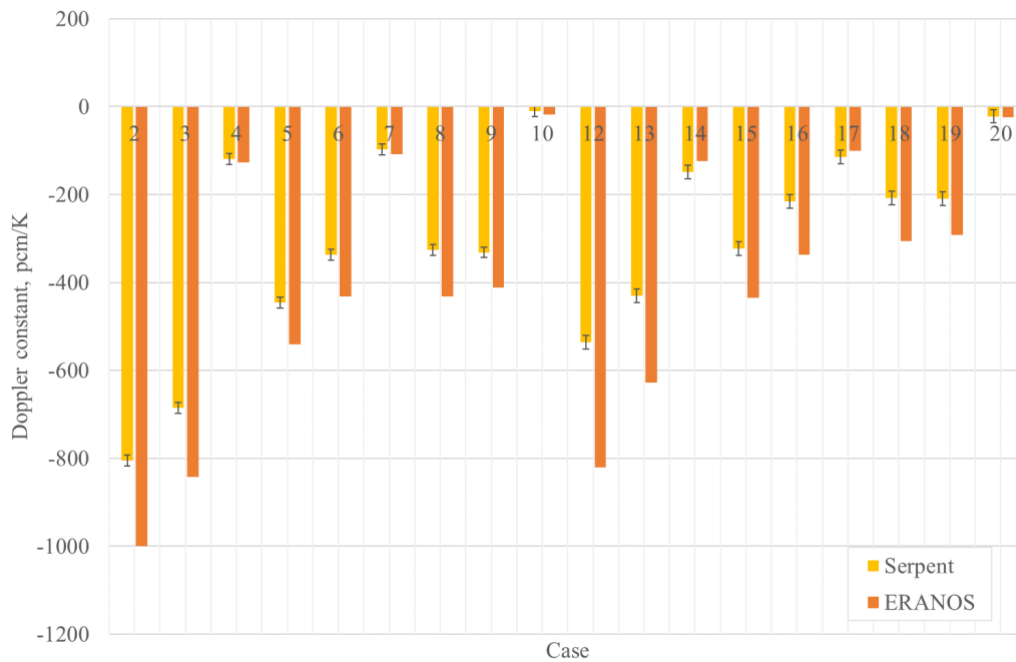


Figure 18 - Doppler constant for coarse mesh, pcm/K

7.2 Local Doppler constant

The local Doppler constant values estimated by Serpent and ERANOS are shown in Fig. 19. Unlike the global results, the Serpent results are more negative with respect to the constants obtained by ERANOS. However, although the statistical uncertainty of the multiplication factor is about 1 pcm, this propagates to about 8 pcm uncertainty on the Doppler constant. The result is that most of the difference observed between ERANOS and Serpent is within the statistical uncertainty.

The relative statistical uncertainty of the estimated coefficient by Serpent increases drastically in the low importance regions (top and bottom of the core, as well as the outer regions). In the inner regions, the relative statistical uncertainty is about 10-20%, while in the outer parts this value can reach more than 100%.

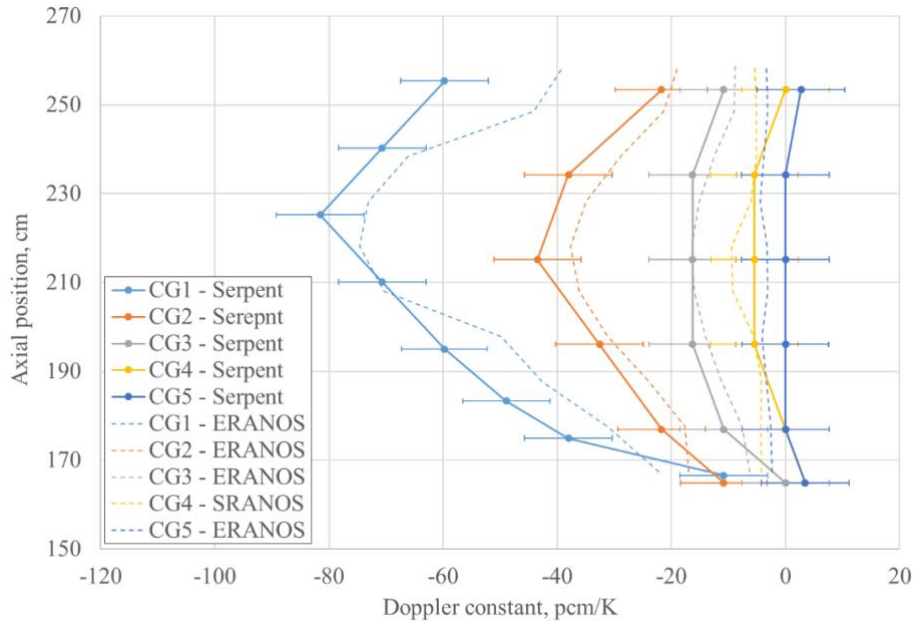
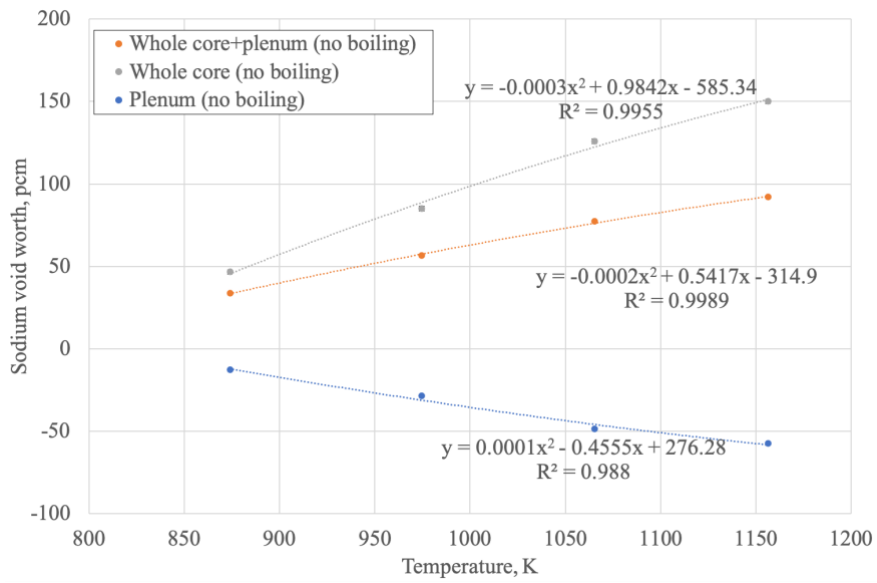
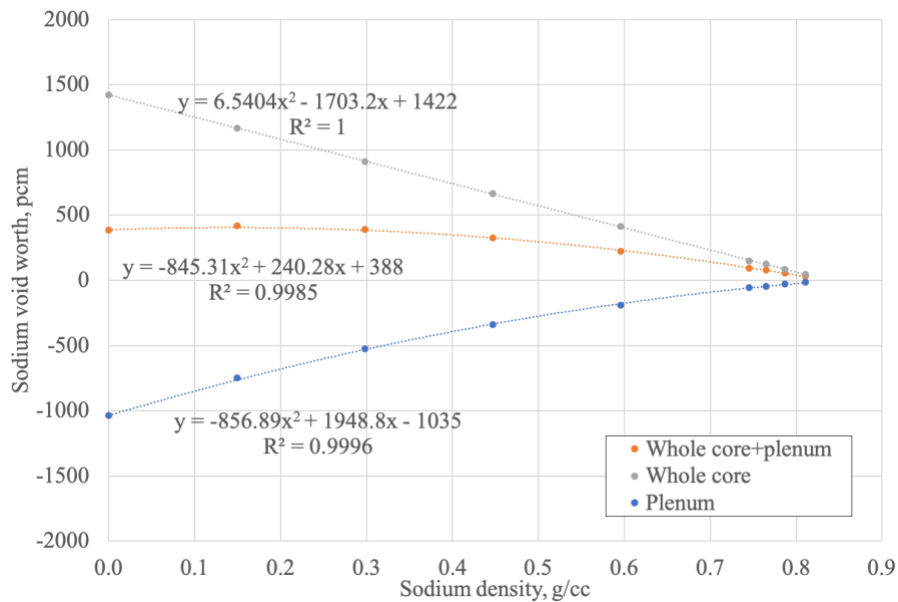


Figure 19 - Local Doppler constants in different radial cooling groups, pcm/K

7.3 Global sodium void worth



(a) Temperature



(b) Sodium density

Figure 20 - Sodium void worth as a function of temperature and sodium density

The sodium void worth behaves linearly as long as no actual boiling occurs in any of the regions, as seen in Fig. 20a. However, this trend becomes less linear in the plenum as sodium starts to boil, while boiling inside the active core region (fissile and fertile zones) remains fairly linear (Fig. 20b). The combination of the two effects results in some deviation from linear behaviour of the core+plenum simulation.

7.4 Local sodium void worth

The local sodium worth map is shown in Fig. 21. The void reactivity worth behaves as expected. In the fissile and fertile zones it is positive while in the plenum zone it is negative. ERANOS results are consistently predicting lower void worth values with respect to those obtained by Serpent in the active core region. The latter follow the trends observed in the zone-wise voiding simulations (Fig. 11), where ERANOS void worth in the active core is consistently lower than the one predicted by Serpent. In the plenum, the two codes agree better, although ERANOS predicts a slightly more negative void worth. This is similar to the results observed in the zone-wise void simulations.

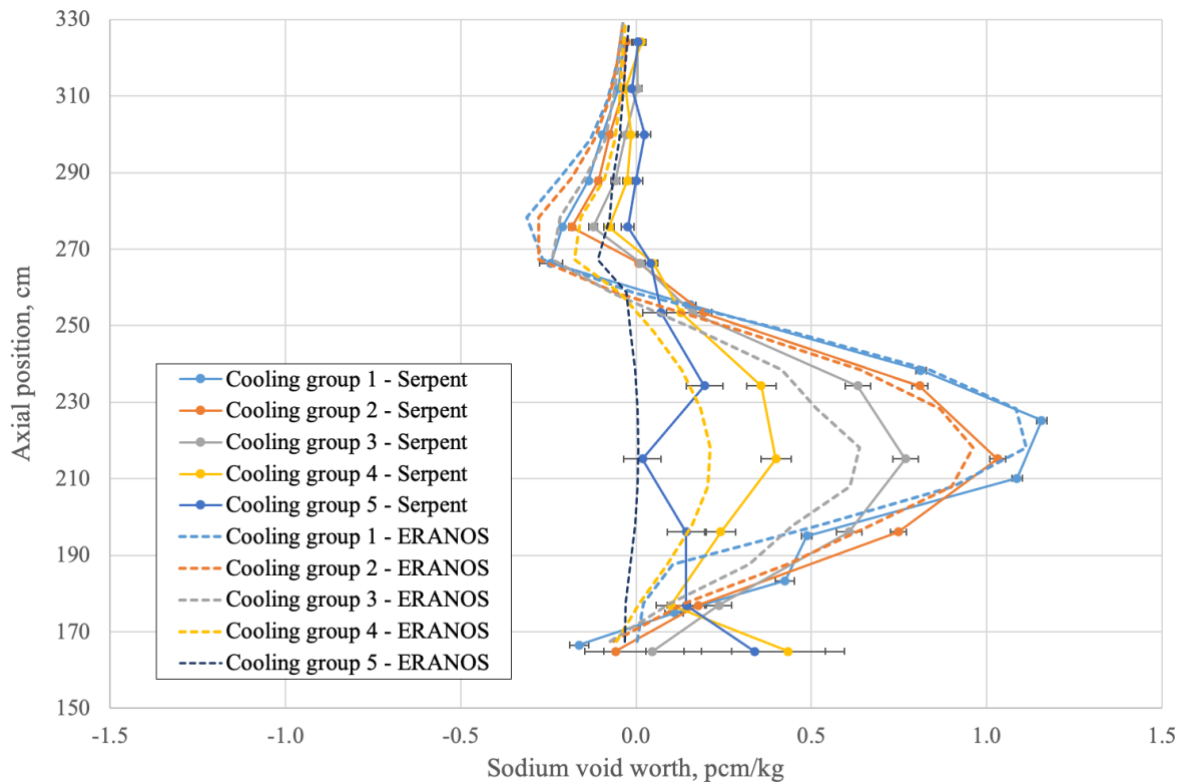


Figure 21 - Local sodium void worth map

It is worth it to highlight that the local sodium void maps in Figure 21 reflect the effect of voiding each region individually, giving rise to the so-called conventional mapping. However, due to the spatial correlations between the active upper core and the sodium plenum explained in Section 5.3, the global effect of voiding two different axial regions will not be necessarily the sum of both individual contributions. Along the ESFR-SMART project, a method based on sensitivity analysis and similarity assessment [18] has been proposed to identify the main spatial correlations between axial zones to be considered in order to provide a more realistic sodium void mapping for transient analyses. A methodology for feeding that realistic mapping to thermal-hydraulic system codes is currently under way.

8 Summary and conclusions

Neutronic modelling of the ESFR core in its EOE state has been completed. Parameters considered include the criticality, control rod worths, and both local and zone-wise analysis of safety-relevant reactivity coefficients. An acceptable level of agreement is observed between the four neutronics codes (Serpent, KENO-VI, WIMS, and ERANOS) used for the analysis, giving confidence in the suitability of these methods and tools for modelling large, commercial-scale SFRs. In cases where a larger discrepancy is seen between Serpent and KENO-VI, the difference can be explained by the lack of probability tables in KENO-VI calculations as detailed in [19]. Although the sodium void worth at EOE is found to be more positive at EOE than at BOC, further study points to this being due to the breeding of plutonium in the fissile zones over time.

Investigations have also been carried out into the global and local analysis of the Doppler constants and sodium void worths. This was done by further discretizing the core with the use of radial

cooling groups and axial segments in order to evaluate the linearity and spatial correlations. The results show the expected more negative Doppler constants and more positive sodium void worths in the central regions. These more detailed maps of the main safety-relevant parameters will serve as basis for the transient calculations planned for the next stage of the work on the ESFR.

Further work on sensitivity and uncertainty analysis, as well as an investigation into the decay heat maps at EOEC, has been performed and is reported in [1, 2].

Acknowledgments

The research leading to these results has received funding from the Euratom research and training programme 2014-2018 under Grant Agreement Number 754501 (ESFR-SMART).

References

- [1] M. Margulis, U. Davies, E. Shwageraus, A. Jimenez-Carrascosa, N. Garcia-Herranz, O. Cabellos, J. Krepel, E. Fridman, R. Gregg, 2020. "Safety and performance parameters at EOC", ESFR-SMART Project deliverable D2.2
- [2] A. Jiménez-Carrascosa, N. García-Herranz, M. Margulis, U. Davies, E. Shwageraus, E. Fridman, R. Gregg, J. Krepel, 2020. "Decay heat characterization for the European Sodium Fast Reactor", *Journal of Nuclear Engineering and Radiation Science*, to be submitted.
- [3] K. Mikityuk *et al.*, "ESFR-SMART: new Horizon-2020 project on SFR safety," in *Proceedings of IAEA FR2017*, 2017.
- [4] G. L. Fiorini and A. Vasile, "European Commission – 7th Framework Programme: The Collaborative Project on European Sodium Fast Reactor (CP ESFR)," *Nucl. Eng. Des.*, vol. 241, no. 9, pp. 3461–3469, Sep. 2011.
- [5] E. Fridman, F. Álvarez-Velarde, P. Romojaro-Otero, H. Tsige-Tamirat, A. Jiménez-Carrascosa, N. García-Herranz, F. Bernard, R. Gregg, U. Davies, J. Krepel, S. Massara, S. Pומרouly, E. Girardi, K. Mikityuk, 2020a. "Neutronic analysis of the European Sodium Fast Reactor: Part I - fresh core results", *Journal of Nuclear Engineering and Radiation Science*, NERS-20-1056, accepted.
- [6] E. Fridman, F. Álvarez-Velarde, P. Romojaro-Otero, H. Tsige-Tamirat, A. Jiménez-Carrascosa, N. García-Herranz, F. Bernard, R. Gregg, U. Davies, J. Krepel, B. Lindley, S. Massara, S. Pומרouly, E. Girardi, K. Mikityuk, 2020b. "Neutronic analysis of the European Sodium Fast Reactor: Part II - burnup analysis", *Journal of Nuclear Engineering and Radiation Science*, NERS-20-1067, accepted.
- [7] A. Rineiski, C. Meriot, C. Coquelet-Pascal, J. Krepel and E. Fridman, "Specification of the new core safety measures," ESFR-SMART, Karlsruhe, Germany, 2018.
- [8] A. Koning, R. Forrest, M. Kellett, R. Mills, H. Henriksson and Y. Rugama, "The JEFF-3.1 Nuclear Data Library," OECD Nuclear Energy Agency, Paris, France, 2006.
- [9] J. Leppänen, M. Pusa, T. Viitanen, V. Valtavirta and T. Kaltiaisenaho, "The Serpent Monte Carlo code: Status, development and applications in 2013," *Annals of Nuclear Energy*, vol. 82, no. September, pp. 142-150, 2015.
- [10] B. T. Rearden and M. A. Jessee, "SCALE Code System," Oak Ridge National Laboratory, Oak Ridge, TN, United States, 2017.
- [11] B. Lindley, G. Hosking, P. Smith, D. Powney, B. Tollit, T. Fry, R. Perry, C. Murphy, C. Grove, M. Thomas, K. Hesketh and D. Kotlyar, "Developments within the WIMS Reactor Physics Code for

- Whole Core Calculations,” in *Proceedings of M&C2017*, Jeju, South Korea, 2017.
- [12] J.-M. Ruggieri, J. Tommasi, J. F. Lebrat, C. Suteau, D. Plisson-Rieunier, C. De Saint Jean, G. Rimpault and J. C. Sublet, “ERANOS 2.1: International code system for GEN IV fast reactor analysis,” in *Proceedings of ICAPP*, Reno, NV, USA, 2006.
- [13] B. Lindley, J. Hosking, P. Smith, D. Powney, B. Tollit, T. Newton, R. Perry, T. Ware and P. Smith , “Current status of the reactor physics code WIMS and recent developments,” *Annals of Nuclear Energy*, vol. 102, pp. 148-157, 2017.
- [14] A. Kavenoky, “The SPH homogenisation method.”,” in *A Specialists’ Meeting on Homogenization Methods in Reactor Physics*, London, 1978.
- [15] G. Rimpault, D. Plisson, J. Tommasi, R. Jacqmin and J. Rieunier, “The ERANOS code and data system for fast reactor neutronic analyses,” in *Proceedings of PHYSOR2002*, Seoul, South Korea, 2002.
- [16] J. Krepel, S. Pelloni, K. Mikityuk and P. Coddington, “EQL3D: ERANOS based equilibrium fuel cycle procedure for fast reactors,” *Annals of Nuclear Energy*, vol. 36, no. 5, pp. 550-561, 2009.
- [17] J. Krepel, S. Pelloni, S. Bortot, A.-L Panadero, and K. Mikityuk, "Mapping of Sodium Void Worth and Doppler Effect for Sodium-cooled Fast Reactors", in *Proceedings of ICAPP*, Nice, France, 2015
- [18] A. Jiménez-Carrascosa and N. García-Herranz. "Use of similarity indexes to identify spatial correlations of sodium void reactivity coefficients." *Nuclear Engineering and Technology* (2020).
- [19] A. Jiménez-Carrascosa, E. Fridman, N. García-Herranz, F. Alvarez-Velarde, P. Romojaro, and F. Bostelmann, “About the impact of the Unresolved Resonance Region in Monte Carlo simulations of Sodium Fast Reactors,” in *Proceedings of ICAPPs*, 2019, p. 15.